In – depth chemical and optoelectronic analysis of triple-cation perovskite thin films by combining XPS profiling and PL Imaging

Stefania Cacovich[†] [(1)], Pia Dally[†] [(2,3)], Guillaume Vidon [(2)], Marie Legrand [(2,4)], Stéphanie Gbegnon [(2)], Jean Rousset [(2,4)], Jean-Baptiste Puel [(2,4)], Jean-François Guillemoles [(1)], Philip Schulz [(1)], Muriel Bouttemy [(2,3)], Arnaud Etcheberry [(3)]

[(1)] CNRS, Institut Photovoltaïque d'Île de France (IPVF), UMR 9006, 18 boulevard Thomas Gobert, 91120, Palaiseau, France

[(2)] Institut Photovoltaïque d'Île de France (IPVF), 18 boulevard Thomas Gobert, 91120, Palaiseau, France

[(3)] Institut Lavoisier de Versailles (ILV), Université de Versailles Saint-Quentin-en-Yvelines, Université Paris-Saclay, CNRS, UMR 8180, 45 avenue des Etats-Unis, 78035 Versailles Cedex, France

[(4)] EDF R&D, Institut Photovoltaïque d'Île de France (IPVF), 18 boulevard Thomas Gobert, 91120, Palaiseau, France

[†] Equal contribution

Keywords: halide perovskites, in-depth chemical analysis, film thinning by Ar^+ ion beam sputtering, X-ray photoelectron spectroscopy, profiling, photoluminescence

ABSTRACT

The investigation of chemical and optoelectronic properties of halide perovskite layers and associated interfaces is crucial to harness the full potential of perovskite solar cells. Depth-profiling photoemission spectroscopy is a primary tool to study the chemical properties of halide perovskite layers at different scales from the surface to the bulk. The technique employs ionic argon beam thinning that provide accurate layer thicknesses. However, it is necessary to verify the reliability of the chemical information considering the fragility of halide perovskite thin films. The present study addresses the question of the Ar^+ sputtering thinning on the surface chemical composition and optoelectronic properties of triple-cation mixed-halide perovskite by combining X-ray photoemission spectroscopy (XPS) and photoluminescence (PL) spectroscopy. First, XPS profiling is performed by Ar^+ beam sputtering on a half-cell constituted of glass/FTO/c-TiO_2/ perovskite. Resulting profiles show a very homogenous and reproducible elements distribution until near the buried interface, therefore the layer is considered as quasi homogeneous all over its thickness and the sputtering process stable. Secondly, we evaluated a set of thinned perovskite layers representative of selected steps along the profile by means of PL imaging optical measurements in both steady-state and transient regimes to assess possible perturbation of the optical properties from surface to bulk. Obtained PL spectra inside the resulting craters show no peak shift nor phase segregation. Accordingly, the transient PL measurements do not reveal any changes of the surface recombination rate in the sputtered areas. This demonstrates that there is no cumulative effect of sputtering nor drastic chemical and optoelectronic modifications, validating the determination of the in-depth composition of perovskite layer. Combining XPS profiling with PL characterization can be a precise tool to be applied for an extensive study of the multiple layers and mixed organic / inorganic interfaces of photovoltaic devices.

INTRODUCTION

During the past few years, hybrid perovskite solar cells have attracted a considerable amount of research and have undergone rapid development as next generation photovoltaics [1,2]. Despite the outstanding power conversion efficiency (PCE), rapidly increasing and exceeding now 25.6 % [3] for a single-junction *n-i-p* device, one of the main drawbacks of this technology remains its intrinsic and extrinsic instability [4,5]. In order to enhance the device performances and stability, not only high-quality perovskite absorber thin films need to be developed but also the optimization of the entire structure and layer stacking of the cell has to be considered. Researchers nowadays are focusing on enhancing the device architecture where interface properties play a crucial role on the final performances and durability [6–10]. In particular, it is of primary importance to understand the physical and chemical phenomena occurring at those interfaces, site of defects accumulation and carrier recombination [11,12], band mis-alignment [13–15] or chemical changes [16–19].

To chemically characterize these nanoscale systems, several advanced characterization techniques were employed and reported in the literature, including scanning transmission electron microscopy / energy dispersive X-ray spectroscopy (STEM-EDX) [20,21], time-of-flight secondary ion mass spectrometry (ToF-SIMS) [16,22–24], glow discharge optical emission spectrometry (GD-OES) [25] and X-ray photoelectron spectroscopy (XPS) [26–28]. However, organic-inorganic materials, such as hybrid halide perovskites, are prone to degradation when exposed to high-intensity or prolonged electron beam [29,30] or ion bombardment [31]. Therefore the potential characterization-induced artifacts need to be carefully assessed [32–35] to ensure the reliability of the analysis. In particular, XPS is a technique primarily used to measure the surface chemical composition of electronic materials, that can be also used in conjunction with ion sputtering to investigate the in-

depth chemical profile of different elemental species [36] by acquiring spectra inside the generated craters. Several groups have already studied the elemental distribution of perovskite components inside the perovskite layers using XPS sputtering methods, using either monoatomic argon (Ar^+) sputtering or argon cluster (Ar_n^+) projectiles. However, Ar^+ and Ar_n^+ sputtering generally causes significant changes to the surface chemistry but may also have effects on the sample composition in depth. Indeed, in the case of perovskite layers, composed of both organic and inorganic species, many artefacts linked to the abrasion process are expected as reported in the literature [31]. In the specific case of triple-cation lead mixed-halide perovskites (Cs, formamidinium $CH(NH_2)_2^+$ [FA], methylamonium $CH_3NH_3^+$, [MA]), that currently yield the highest solar cell efficiency, only few publications focus on the effects of the sputtering [37] . The complexity of the chemical composition of such compounds makes this kind of measurements even more challenging. One of the main limitations resides in the systematic reduction of Pb^{2+} species in Pb^0 in the sputtering process, obfuscating an accurate description of the metallic element's oxidation state inside the layer along with the exact amount of oxygen incorporation. Busby et al. performed a systematic study of the evolution of the Pb^0/Pb^{2+} ratio for triple-cation perovskite layers when changing the sputtering method [31]; Ar^+ or Ar_n^+ [33]. They showed that, in their case, the Pb^0 content increases with the sputtering time and it is affected by the beam conditions, such as cluster size and kinetic ion energy.

Once again, the reliability of this characterization approach combining sputtering and XPS analysis is crucial. Several factors should be taken into account including the sensitivity of the material but also the Ar^+ sputtering itself that might induce the creation of artefacts, among them preferential etching and surface elements redistribution [38,39].

The major question this article focuses about is: does profiling generate perturbations and degradation of the perovskite in bulk from an optoelectronic point of view?

In this work, the impact of monoatomic Ar^+ sputtering on triple-cation perovskite layers is explored on half cells. The question of the in-depth redistribution of the elemental components as a function of the perturbation is essential. Both chemical and optical modifications are studied for different sputtering times to have a better understanding on the sputtering process and the level of the eventual induced perturbation.

XPS gives information about the nature and the intensity of the perturbation in the top-most layer, typically throughout a thickness of 5 nm, but does not elucidate on possible modification to the sample underneath. In parallel, photoluminescence (PL) is a versatile probe to investigate the optoelectronic properties, both at the surface and in the bulk. We use the technique to quantify the energy gap (E_g), radiative vs non-radiative recombination rates and diffusion length, making it possible to probe optical variations. In the present case, with highly-absorbed excitation wavelengths, the ultimate depth probed is comprised within 50 to 100 nm, which is much larger than the one of XPS, thus, combining XPS and PL is in evident interest to assess the in-depth composition and / or the changes induced by the bombardment that could range deeper into the perovskite layer, and correlated the optoelectronic properties to the compositional changes.

HAXPES (Hard X-ray PhotoElectron Spectroscopy) would bring additional information about deeper changes in the composition and an assessment of the damaged overlayer thickness [40] but it is limited by the stability of the perovskite layer under the high energy X-Ray radiation. The approach proposed here, with the complementary use of XPS and PL, aims at yielding a reliable diagnosis of the surface modifications of the irradiated perovskite as well as an evaluation of the in-depth perturbation. The impact of Ar^+ ion bombardment on the perovskite layers is accurately studied following the possible damages that can be induces in term of surface morphology, composition and optoelectronic properties. In practice, the surface is etched by rastering the ion

beam over a square or rectangular area of 2 mm^2 dimension compatible with XPS spot size (here almost 400 µm in the bigger diagonal). Information about the surface evolution of the perovskite film during Ar^+ profiling will be assessed by varying the sputtering time from 120 s to 720 s, and thus, the corresponding remaining thickness of perovskite. The comparison enables us to determine if the induced modifications are amplified with the sputter duration. For each abrasion step, the surface composition and chemistry are measured and the optical and transport properties of the halide perovskite layer investigated by using photoluminescence imaging methods operating in both steady-state and transient regimes.

RESULTS AND DISCUSSION

This study was realized on a half-cell constituted of a stack of glass / fluorine doped tin oxide (FTO) / compact titanium oxide (c-TiO_2) / triple-cation double halide perovskite with a nominal stoichiometry of $Cs_{0.05}(MA_{0.14}, FA_{0.86})_{0.95} Pb(I_{0.84}, Br_{0.16})_3$. The high sensibility of the perovskite layers requires specific care for sample handling and transfer procedures from the glove box, where the films are deposited, to the analysis tools for the chemical and optical characterization. Half cells were transferred to the XPS spectrometer chamber under inert atmosphere, and this same transfer procedure was also applied for optical characterizations. Preliminary XPS analyses were then realized to determine the optimal operating condition [36], ensuring the stability of those layers and the reliability of the chemical and optoelectronic measurements. XPS analyses were carried out to verify the samples composition and stoichiometric conformity, their lateral homogeneity, as well as their stability after one-hour exposure to X-rays under ultra-high vacuum (UHV) atmosphere. The chemical homogeneity of the perovskite layer surface was verified, using multipoint mode analysis, by performing the analysis on 5 random point on each sample and

repeated on 4 sets of samples (**Figure S1)**. This preliminary study demonstrates that the surface of the samples is chemically uniform, very essential result for the choice of the analysis area for the subsequent optical characterization.

Moreover, the comparison between the initial atomic percentages for the as-deposited perovskite layer and after 1 hour of X-rays irradiation **(Table S1)** shows no significant change in the element's contents nor a modification in the photopeak shape (not shown here) indicating the absence of changes to the chemical environments. This ensures that the XPS measurements are well representative of the perovskite surface without beam damage effects.

The effect of the Ar^+ ion bombardment on the chemical and optoelectronic properties was studied on a set of sputtered half cells prepared inside the XPS analysis chamber using the ion gun in monoatomic mode (Ar^+ projectiles) with an energy of 1000 eV and current of 10 nA. A schematic of the process is reported in **Figure 1a**. For the next optical characterizations, the morphology of the perovskite film inside the crater remains a critical property. To that end, we compared the morphology of a pristine perovskite thin film with the one of a film after 240 seconds Ar^+ sputtering by using both scanning electron microscopy (SEM) and atomic force microscopy (AFM). As expected, the initial pristine perovskite films exhibit full surface coverage with a uniform grain structure and size of 150 – 200 nm (**Figure 1b**). After the sputtering process, a slight preferential orientation of the surface morphology is induced due to the ion gun geometry and the grain boundaries are no more distinguishable in the SEM image. However, we do not observe any features of local morphological degradation or pinholes (**Figure 1c**). After sputter-profiling lines we observe the appearance of lines in the images. These are part of the actual surface

morphology and stem from the depth profiling geometry for which the Ar^+ cluster gun is oriented at an angle of 30° with respect to the sample surface normal.

In agreement with SEM results, AFM images show a clear modification of grain size after Ar^+ sputtering and the grain boundaries become blurred. The root mean square (rms) were measured after prolonged sputtering sequences (up to 600 seconds), and reported in SI, **Table S2,** for each corresponding remaining thickness. The same morphology post-sputtering was observed confirming that the conditions employed did not lead to significant changes in the morphology, and especially the surface roughness as the rms values remain the same, around 17 nm. This insignificant change in roughness of the Ar^+ sputtered zone suggests that the optical reflectivity inside these craters remains unmodified throughout the sputtering process.

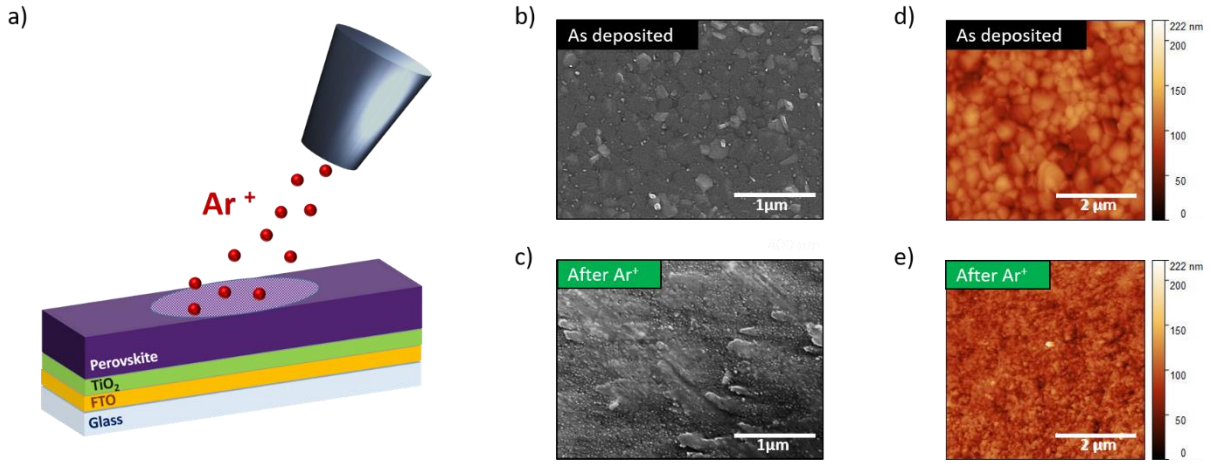

Figure 1. Effects of Ar^+ sputtering on sample morphology. a) Schematic of the sputtering process. SEM images of perovskite thin films before b) and after c) Ar^+ sputtering for 240 s and corresponding AFM surface 3D mapping of perovskite thin films before d) and after e) Ar^+ sputtering.

XPS profiling through the entire thickness of the half device was realize to determine the total duration of the sputtering sequence to reach the perovskite / TiO_2 interface, positioned at 420 seconds etching time **(Figure 2 h)**. This time is very reproducible and was verified on ten samples, allowing us to define the remaining thickness of perovskite for each sputtering time for a quantitative thinning of the layers. Then, 7 additional samples were prepared by implementing sputtering times between 60 s and 720 s to analyze the surface state at different stages of the profiling process (**Table 1**). For each crater, XPS survey spectra were recorded in order to plot the chemical distribution of elemental components for each sputtering time. The evolution of the atomic percentage of the elements present inside the craters resulting from different sputtering durations on 8 different samples (i.e. different residual perovskite thicknesses) are presented in **Figure 2.** By comparing the set of profiles obtained, we confirm the remarkable reproducibility of the profiling process.

Crater number	Sputtering conditions	Estimated remaining thickness [nm]
1	2 levels / 60 seconds	350 ± 20
2	4 levels / 60 seconds	250 ± 20
3	5 levels / 60 seconds	200 ± 20
4	6 levels / 60 seconds	150 ± 20
5	7 levels / 60 seconds	100 ± 20
6	8 levels / 60 seconds	Interface perovskite /TiO_2
7	9 levels / 60 seconds	Interface perovskite /TiO_2
8	12 levels / 60 seconds	Interface perovskite /TiO_2

Table 1. Description of the sputtering conditions and estimation of the perovskite remaining thicknesses for different sputtering times.

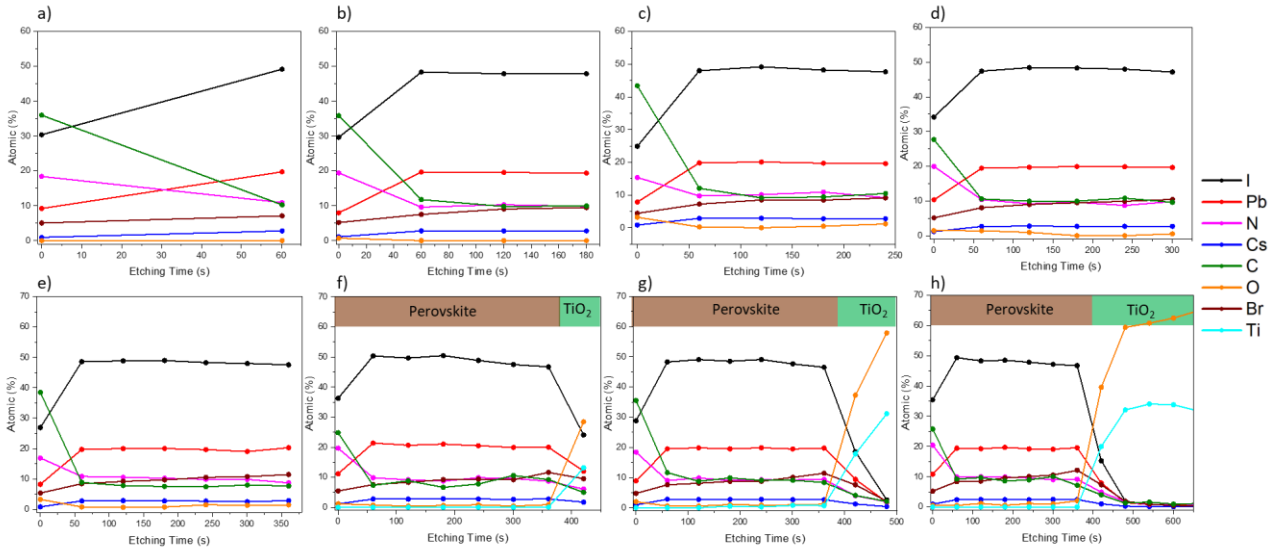

Figure 2. XPS depth profile (Ar^+,1000 eV)) of FAMACs perovskite for the a) crater 1, b) crater 2, c) crater 3, d) crater 4, e) crater 5, f) crater 6, g) crater 7 and h) carter 8. Quantification has been made peak fitting in the Br 3d, Cs 3d, I 3d, C 1s, N 1s, Pb 4f, O 1s and Ti 2p regions. Lateral bars on the top of panels f-h indicate the transition from the perovskite layer to the TiO_2 substrate.

Except at the extreme surface, where we measure the carbonaceous contamination layer, which is removed after the first 60 s of etching, the I, Pb, N, Cs and C contents in depth are quasi stable. However, we observe the accumulation of Br at the perovskite / TiO_2 interface in agreement with ToF-SIMS profiling of triple-cation perovskite devices already reported in the literature [22,41,42].

The elements distribution is remarkably similar inside the perovskite layer irrespective of the chosen crater, thus further corroborating the reproducibility of the sputtering process and the homogeneity in the bulk of the perovskite layer. This finding means that the following PL characterization will probe for every crater, a chemically homogenous layer.

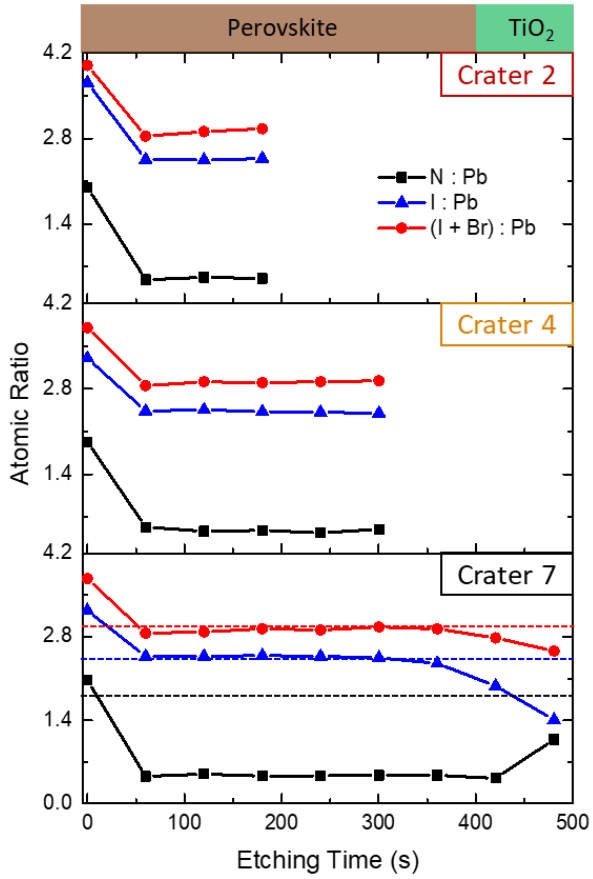

Figure 3. Atomic ratio of N : Pb, I : Pb and (I+Br) : Pb for crater 2 (remaining thickness 250 nm), crater 4 (remaining thickness 150 nm) and crater 7 (Perovskite / TiO_2 interface). The dashed lines indicate the corresponding theoretical ratios.

In **Figure 3**, we reported the calculated atomic ratios N : Pb, I : Pb and (I + Br) : Pb for crater 2 and 4 whereas the remaining thicknesses are respectively 250 nm and 150 nm, and crater 7 which lays bare the interface region between the perovskite film and the TiO_2 substrate. In the perovskite structure $(Cs_{0.05}(MA_{0.14}, FA_{0.86})_{0.95}\,Pb\,(I_{0.84}, Br_{0.16})_3)$, the theoretical atomic ratio N : Pb should be equal to (1.8 : 1), while the atomic ratios I : Pb and (I + Br) : Pb should be equal to (2.5 : 1) and (3 : 1), respectively. At the perovskite surface, experimental ratios show values which are close to

the expected ideal stoichiometry with a slight iodine and nitrogen enrichment. Previous trends observed on the atomic depth profiles are confirmed by comparing the evolution of the corresponding ratios. In these craters, the three ratios show an abrupt decrease after the first 60 seconds of sputtering varying from ~ 2.0 to 0.5 for N : Pb, from 4 to 3 for (I + Br) : Pb and from 3.7 to 2.4 for I : Pb, corresponding to the removal of the carbon contamination as well as the Pb enrichment inside the layer. Subsequently, the composition remains almost stable until 300 s of sputtering. Finally, when approaching the perovskite/TiO_2 interface, noticeable modifications are observed, with a gradual drop of the I : Pb and (I + Br) : Pb ratios from 2.4 to 1.4 and from 3 to 2.5 respectively. This evidences an interface where the concentration of iodine is low while it is rich in Br. Finally, a specific halide distribution is shown, with an accumulation of iodine at the perovskite surface and of bromine at the bottom, i.e. at the perovskite / TiO_2 interface. Similar findings were reported on triple-cation mixed-halide perovskite layers by different groups [9,28,29] which showcases the reproducibility of XPS profiling technique on such absorbers. Undoubtedly, the reproducibility of the ratio evolution, whatever the etching time, allow to assume a high level of homogeneity of the perovskite film from the top surface to the interface.

Additional XPS high-resolution spectra of Pb 4f, N 1s, C 1s, I 3d and Br 3dcan be found in **Figure S2** for the fresh perovskite (Ref) before sputtering, and for 3 different sputtering times on 3 different spots of the samples, for crater 2, 3 and 4 whereas the remaining thicknesses are respectively 250 nm, 200 nm and 150 nm. After the first 60 s of etching (crater 2), the formation metallic lead is visible on the Pb 4f spectra, indicating the reduction of Pb^{2+} to Pb^0. The formation of metallic lead has been observed before as a presumed degradation product in halide perovskite

samples. However, this amount of Pb^0 remains the same after 120 s (crater 3), and 180 s (crater 4) of etching.

High-resolution spectra of N 1s and C 1s reported in **Figure S2** also shows that the MA^+ contribution fully disappears after the first 60 s of sputtering, while the FA^+ contribution decreases at a lower rate due to the C – N chemical bond degradation. However, after the first 60 s of sputtering, the N 1s and C 1s peaks remain steady, meaning that the same amount of N and C remains present for crater 3 and 4, and that is until reaching the interface. These stoichiometric changes detected for crater 1 after the first etching remain the same in crater 2 and 3. This implies that the craters 1 to 5 (before the interface) are chemically identical and show the exact same degradation of the organic compounds and formation of metallic lead Pb^0. Therefore, the PL characterization will be then performed on chemically identical surfaces. Moreover, the elemental distribution inside the different craters being exactly the same, we can also confirm that in-depth, the material is also identical. The observed degradations through XPS are restricted to the extreme surface after each sputtering, implying that this is not constraining for the PL characterization which probes the whole perovskite layer.

At this point, it is difficult to discriminate between a perturbation only at the extreme surface or extended more or less beneath the XPS probed thickness. The PL characterization inside the craters shown in the following will allow to determine whether perturbations are detected beneath this probed thickness.

To determine the optoelectronic properties of the perovskite bulk from the craters previously characterized by XPS, we employ a multi-technique PL imaging approach. This includes a combination of both steady-state and transient measurement techniques, namely hyperspectral

imaging (HI)[43] and time-resolved fluorescence imaging (TR-FLIM) [44], we explored the impact of Ar^+ sputtering on the optoelectronic properties of triple-cation mixed-halide perovskite thin films.

Specifically, we performed the HI analysis on a series of craters with an estimated remaining thickness ranging from 250 nm to 50 nm. The measurements were conducted in nitrogen atmosphere, by using a blue LED (450 nm) at an illumination power of approximately 10 suns, i.e. 1W/cm². In **Figure 4a**, we report a series of PL spectrum images, displaying the integrated absolute PL intensity in a reference sample and in five craters (estimated thicknesses around 250 nm, 200 nm, 150 nm, 100 nm and 50 nm). All the acquisitions were performed in center of the craters to ensure a constant thickness of the perovskite layer, as shown in **Figure S8**. The corresponding PL spectra are shown in **Figure 4b**. The progressive removal of thin layers of perovskite (approximately 50 nm for each step) corresponds to a decrease of the PL peak intensity. Importantly, we did not observe the emergence of new phases as the shape of the PL spectra does not critically vary. However, the drop of the PL peak intensity can be ascribed to several factors.

First, the reduction of the thickness of the triple-cation perovskite layer should result in a stepwise decrease of the PL peak intensity (see modeling details in SI). Additionally, an increase of non-radiative recombination centers and creation of defects induced by Ar^+ sputtering which therefore provoked the deterioration of the optoelectronic properties of the materials could also be a cause for the PL peak intensity reduction.

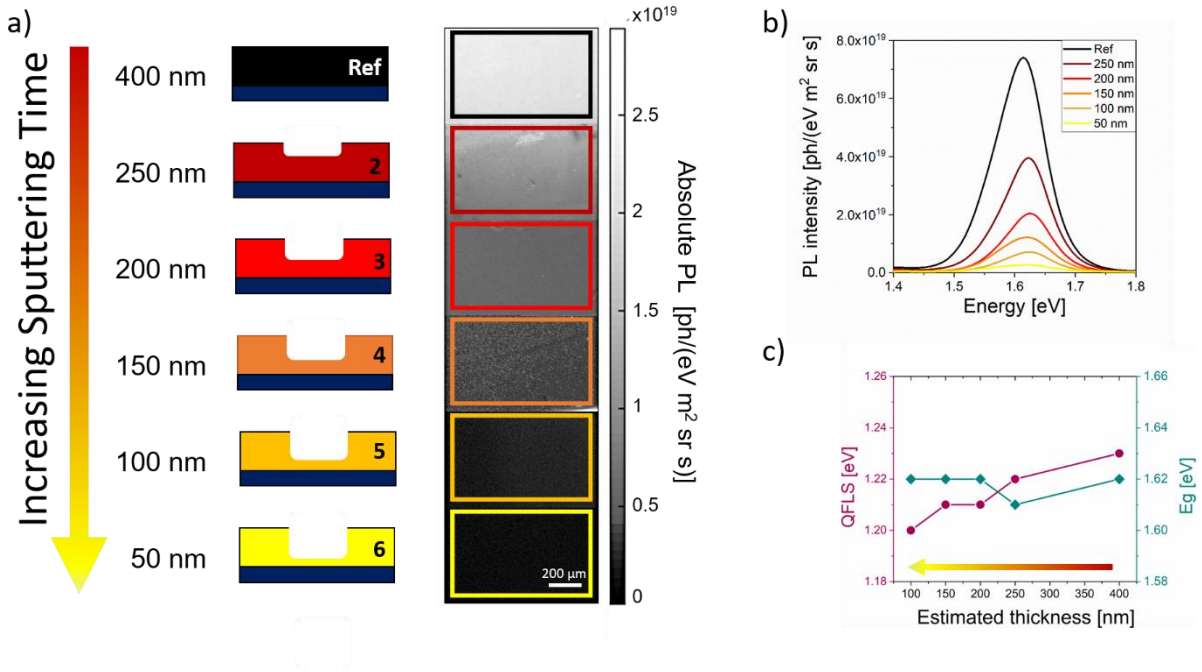

Figure 4. Photoluminescence imaging analysis. a) Series of PL spectrum images acquired on craters formed after different sputtering times. b) Average PL spectra of selected zones in the craters c) Quasi Fermi level splitting and energy gap variations as a function of the estimated thickness of the perovskite layer.

To address this question, we employed a physical model based on Planck's law[45] which allows to determine the main parameters governing the optoelectronic properties of a semiconductor:

$$I_{PL}(E) = \frac{2\pi}{h^3c^2}\frac{E^2 a(E)}{\exp\left(\frac{E-\Delta\mu}{kT}\right)-1}$$

where h is the Planck constant, c is the speed of light, E is the photon energy, a(E) is the photon energy dependent absorptivity of the sample, $\Delta\mu$ is the quasi-Fermi level splitting, and kT is the thermal energy of the charge carriers.

Estimated Remaining Thickness [nm]	Absorption coefficient times thickness α x d [a.u.]	QFLS [eV]	E_g[eV]
400	5	1.23± 0.01	1.62± 0.01
250	3.125	1.22± 0.01	1.61± 0.01
200	2.5	1.21± 0.01	1.62± 0.01
150	1.875	1.21± 0.01	1.62± 0.01
100	1.25	1.20± 0.01	1.62± 0.01

Table 2. Values of the main parameters calculated with PL fitting for different estimated thicknesses in the perovskite layer.

We thus fitted the PL spectra and quantitatively assessed the evolution of key materials properties such as the energy gap (E_g) and the quasi-Fermi level splitting (QFLS). Fitting results for the PL spectrum relative to crater 6 (nominal thickness 50 nm), are not reported as the signal-to-noise ratio (SNR) was too low to perform a reliable analysis. This can be ascribed to the fact that for this crater the interface with the TiO_2 was reached and hence the PL signal was too weak. The results of the fitting procedure are reported in **Table 2**. In the model we considered the absorption coefficient α to be constant, whereas we varied thin film thickness d by following the sputtering time. The product α x d is therefore directly proportional to the estimated remaining thickness. We determined the QFLS to vary from 1.23 eV in the neat sample to 1.20 eV for 100

nm perovskite thickness (**Figure 4c**). Despite the QFLS values is decreasing of 30 meV, we can still consider that the perovskite exhibits high QFLS values and homogenous optoelectronic properties. Moreover, this is also indicative of a low surface recombination rate, even after the Ar^+ sputtering. Indeed, all the PL maps are rather uniform and do not show any evident morphological degradation. The minimal drop of the QFLS might be ascribed either to a slight degradation of the perovskite layer or to an inaccurate estimation of the thickness that might induce an error in the QFLS calculation on the order of few tens of meV. However, this is a clear indication that the Ar^+ sputtering did not significantly affect the bulk properties of the perovskite film underneath while the surface recombination rate remains low. Moreover, E_g is not shifting, suggesting that no optically active new phases have been formed during the sputtering process.

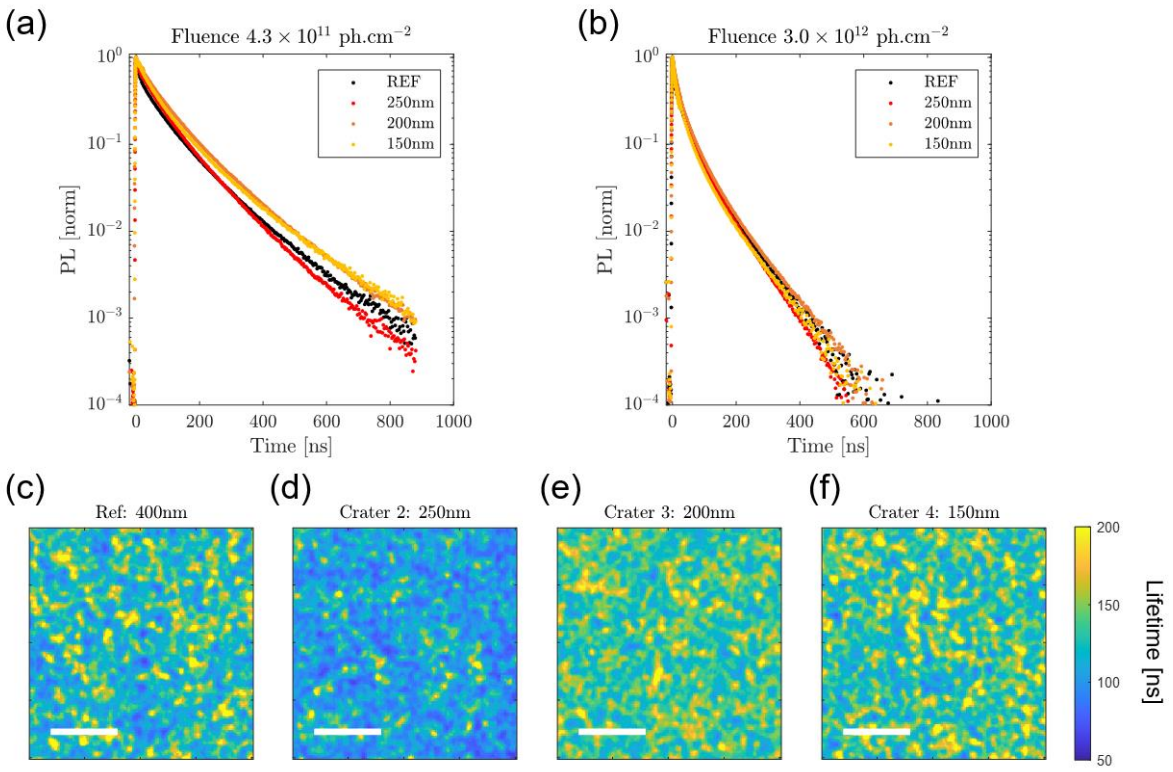

Figure 5. TR-FLIM acquisition. (a) Time resolved decays at a fluence of 4.3e11 ph.cm^{-2} (~40 suns) for the reference and three craters. (b) Similar, for the highest fluence 3.0e12 ph.cm^{-2} (~300 suns). (c-f) Lifetime maps obtained by exponential fitting of the decays in the interval [400,600] ns. The white bar is 50 µm wide.

Complementary information about physical properties within the different craters can be obtained by time-resolved photoluminescence (TR-PL). While steady-state photoluminescence mainly probes the bulk properties of a semiconductor material, transient measurements allow for a more accurate analysis of surface recombination phenomena[46], which are critical in the context of surface chemical analysis such is the case for XPS spectroscopy. We thus performed TR-FLIM analysis for the neat perovskite samples as well for a series of sputtered samples where the etching time was the same used in the Hyperspectral study, corresponding to decreasing thicknesses.

Experiments were conducted in nitrogen atmosphere and with a 532 nm pulsed laser. To compare the excitation intensities with the continuous wave experiment we use the following convention: we consider that 1 sun illumination for the pulsed experiment corresponds to a photo-generated carrier density of approximately 10^{15} cm^{-3} just after the pulse. If we assume an absorption coefficient of $\alpha \sim 10^5$ cm^{-1} then a fluence of 10^{10} $ph.cm^{-2}.pulse^{-1}$ corresponds approximately to 1 sun.

In **Figure 5**, decays averaged over regions inside craters are plotted for the different crater thicknesses. Both decays at low fluence (40 suns, **Figure 5a**) and high fluence (300 suns, **Figure 5b**) are displayed. First, we observe that most of the decays qualitatively correspond to the decay measured for the reference sample. For crater 2 (250 nm), 3 (200 nm) and 4 (150 nm) we observed no radical changes on the decay – indicating that the quality of the top interface of the etched zone is not far from the quality of the un-etched perovskite. At high fluence, radiative recombination plays a significant role. With the high fluence curves, we see that the difference between etched craters and the reference is even reduced: this corroborates the idea that the radiative recombination was not modified by etching, compatible with a similar crystalline structure. Thus, Ar^+ etching seems to only slightly modify the chemical state of the surface of the perovskite, and we have no indication of a modification of the radiative properties. In **Figure 5c** effective lifetime maps are displayed at the 200 µm x 200 µm scale for the reference as well as for the craters 2 to 4 (250 nm to 150 nm thickness). The lifetimes were obtained by fitting local decays in the interval [400, 600] ns for acquisition at 40 suns excitation intensity. We find 129±28 ns for the reference, 108±20 ns for Crater 2 (250 nm), 138±20 ns for Crater 3 (200 nm), and 138±26 ns for Crater 4 (150 nm) for the average and standard deviation of the lifetime over the images. We observe that no major lateral inhomogeneity appears after etching. Moreover, the PL decay times over the films seem

similar from the reference to the craters, indicating that Ar^+ etching did not induce massive recombination at the surface. A comparison with the PL intensity maps just after the laser pulse, as well as the histograms of values for the lifetimes are shown in **Figure S7**.

In order to quantify the impact of Ar^+ etching on the perovskite layers, we fitted decays in the craters them by using a drift-diffusion model[47]. We fixed the bulk non radiative recombination coefficient to a constant (and not fitted) value, $k_1 = 10^6\ s^{-1}$ from previous analysis on our reference perovskite layers [48]. By fixing k_1, we allow for the interpretation of the changes observed in the decays as well as changes of the top surface recombination, as both of these parameters are usually correlated when fitting TR-PL decays. The impact of the value of k_1 on fitting result is discussed in **Figure S4.** We fit the top surface recombination velocity (S_{top}, [$cm.s^{-1}$]), while taking as input the thicknesses and fluences corresponding to each case. The surface recombination velocity is fitted for 4 datasets, each containing one curve for each fluence (3 fluences in total): the reference one, crater 2, crater 3, crater 4. Results are presented in **Figure S3.** On the left part of the figure, the decays and the fitted model are plotted, showing good agreement over all fluences and craters. On the right hand the variations of the top surface recombination parameter are displayed. We find a slight decrease from 160 $cm.s^{-1}$ for the reference to 40 $cm.s^{-1}$ for the 150 nm thick layer. It is surprising to observe this reduction of recombination at the top surface after etching as one could expect that the surface was damaged in the process leading to a higher amount of recombination centers, i.e. undercoordinated Pb. This result is compatible with the hyperspectral imaging measurement we performed, and notably with the fact that the quasi–Fermi level splitting was not substantially modified by the Ar^+ etching. Overall, we note that the Ar^+ etching employed here does not appear to damage the electronic properties of the surface of the triple-cation lead mixed-halide perovskite films, which is a major finding.

CONCLUSIONS

To conclude, in this work we have extensively investigated the impact of Ar^+ sputtering on triple-cation mixed-halide perovskite thin films to verify the reliability of in-depth XPS profiling, commonly used for the chemical characterization of solar devices. In particular, we probed both chemical and physical properties of the material by coupling in-depth XPS analysis and PL imaging techniques. In this way, we determined the influence of the ion impingement on physical parameters such as the energy gap of the material or the carrier lifetimes, proving that these material properties did not significantly evolve after the sputtering process. Thanks to this combined approach, we were able to show that XPS profiling analysis provides reliable chemical information on triple-cation perovskite thin films average composition and does not critically alter the optoelectronic properties of the material at both bulk and surface level.

We quantified the evolution of the main parameters governing the optoelectronic and transport properties of perovskite layer, observing small changes in both steady-state and transient measurements after consecutive Ar^+ etchings. Specifically, the QFLS varied from 1.23 eV in the pristine samples to 1.20 eV close to the absorber / TiO_2 interface, whereas the E_g did not shift from the initial values of 1.62 eV during the whole sputtering process. Moreover, both carrier lifetimes and surface recombination rate did not dramatically change after the ion irradiation. The study of perovskite layers extracted after different increasing sputtering durations, enables to conclude that there are no cumulative effects induced by a prolonged impingement of ions onto the sample surface on the bulk properties of the material as well as no evident surface modifications. This analysis suggests that the Ar^+ sputtering is a reliable technique for probing the in-depth chemical composition of triple-cation perovskite and that it could be extended to compositional studies of other beam-sensitive materials. Finally, a deeper understanding of the impact of the X-rays on the

materials properties can further improve the level of reliability of in-depth XPS profiling method, validating photoemission-based techniques as a powerful tool in the investigation of the chemical composition of novel beam-sensitive complex compounds. Such kind of analyses have already proven to be essential to evidence the segregation phenomenon during ageing or induced by interfaces layer integration steps, understand the phenomenon beyond and break down the barriers limiting at present the stability and efficiency of this emerging technology of solar cells.

EXPERIMENTAL SECTION

Sample preparation

Fluorine-doped tin oxide (FTO) covered glass substrates (Solems) were cleaned by etching with Zn powder and HCl (4M). The substrates were sonicated for 1 hour in an RBS detergent solution (2 vol %), rinsed with deionized water and ethanol, ultrasonicated in ethanol and dried. A TiO_2 electron blocking layer was prepared by atomic layer deposition. The substrates were UV–ozone cleaned for 20 min and transferred into a nitrogen-filled glovebox for the perovskite film deposition. A double cation perovskite solution $(MA_{0.14}FA_{0.86})Pb(I_{0.84}\ Br_{0.16})_3$ was prepared by dissolving 1.10 M PbI_2 (TCI Chemicals), 0.20 M $PbBr_2$ (Alfa Aesar), 1.00 M formamidinium iodide (FAI, Dyesol) and 0.20 M methylammonium bromide (MABr, Dyesol) in a mixture of DMSO:DMF (4:1 in v/v) as solvent. In order to obtain the triple-cation perovskite, i.e. $Cs_x(MA_{0.14}FA_{0.86})_{1-x}Pb(I_{0.84}Br_{0.16})_3$, the required quantity of Cs^+ was additionally injected from a precursor solution of CsI (Sigma Aldrich) 1.50 M in DMSO solvent. The solution, after 2 hours of stirring in a magnetic mixer, was spin-coated onto the TiO_2 layer by following a double plateau. First, 35 µL of the perovskite solution were spincoated at the rotation of 2000 rpm for 10 seconds

at an acceleration of 1000 rpm/s. Then, 100 µL of chlorobenzene were spin-coated at the speed of 6000 rpm for 30 seconds. After deposition, the perovskite films were submitted to an annealing treatment at the temperature of 100 °C for 30 min in a nitrogen glovebox. The thickness of the perovskite thin films is approximately 400 nm.

Morphology characterization

SEM images were acquired by using a Zeiss Merlin Scanning Electron Microscope operating at an acceleration voltage of 20 keV.

AFM images was acquired by atomic force microscopy (Agilent 5600LS) in tapping mode.

X-ray photoelectron spectroscopy (XPS)

Sample architecture consists of a half-cell taken from a n-i-p perovskite solar cell structure: FTO / c-TiO_2 / $Cs_{0.05}(MA_{0.14}, FA_{0.86})_{0.95}$ Pb $(I_{0.84}, Br_{0.16})_3$). To ensure the reliability of the analyzes, freshly synthetized perovskite samples were transferred to the XPS spectrometer in dark and under inert atmosphere conditions, preventing from humidity and light modifications. XPS surface chemical analyzes were carried out with a Thermo Electron K-Alpha$^+$ spectrometer using a monochromatic Al-Kα X-Ray source (1486.6 eV). The Thermo Electron K-Alpha spectrometer procedure was used to calibrate the spectrometer and verified using Cu and Au samples following the ASTM-E-902-94 standard procedure. The X-ray spot size is 400µm. High energy resolution spectra were acquired using a Constant Analyzer Energy (CAE) mode of 20 eV and 0.1 eV as energy step size, without charge compensation. The energy scale was calibrated with respect to the C1s peak settled at 284.6 eV to facilitate comparison of chemical shifts between the various samples investigated. Sputtering was performed with Ar^+ monatomic ions at an energy level of

1000 eV and 10 mA current density with an ion gun orientation of 30°. Data were processed using the Thermo Fisher scientific Avantage© data system. The acquisition sequence for surface analysis was optimized to limit the X-ray irradiation exposure (1 hour) and the stability of the perovskite layer was controlled by recording two survey spectra: one at the start of the acquisition sequence and one at the end (CAE of 100 eV and 1.0 eV energy step size). Three sets of samples were measured to obtain statistic data and guarantee the reliability of the information obtained.

Hyperspectral Imager

The hyperspectral imaging system records a luminescence intensity signal along three dimensions {x,y,λ}. The set-up is composed by a home-built microscope with Thorlabs optomechanical elements, a 2D bandpass filtering system from company Photon Etc with 2 nm resolution, and a 1Mpix silicon-based CCD camera PCO1300. The sample was illuminated with a LED (λ = 450 nm) through a x10Nikon objective with numerical aperture of 0.25, and the luminescence was collected through the same objective. The excitation beam and luminescence signals were separated with appropriate Thorlabs dichroic beam splitter (DMLP 490R) and a FELH 500 filter. The 2D luminescence signal was corrected for each pixel of the sensor from the spectral transmissions along all the optical path, from the read noise and dark current noise of the camera. All the acquisitions were performed in nitrogen atmosphere. Post-treatment of the data cubes includes a deconvolution and fit to the generalized Planck law, which are realized with a dedicated Matlab routine employing the Levenberg−Marquardt algorithm.

TR-FLIM

The TR-FLIM setup records luminescence intensity over an imaging sensor and as a function of time. We used a Princeton Instrument PiMAX4 gated camera. We used 3ns wide temporal gates that we slid in time to record the local decays of the films. The illumination was performed with a Coherent Laser (λ = 532nm, pulse width 15 ps), defocused and homogenised by a rotating diffuser to obtain a flat and homogenous wide field excitation. The repetition rate of the laser was set to 40kHz. To estimate the fluences, the wide field illumination was imaged with a portable CCD array to obtain the illumination area while the incident power was also measured. A x10 objective was used both for excitation and collection, and the laser was filtered out with a DMLP650R beam splitter as well as with a FEL0680 filter. High temporal resolution (time between gates: 120ps) acquisitions as well as regular resolution (time between gates: 3ns) were performed.

ASSOCIATED CONTENT

Supporting Information

The supporting information contains: High-resolution XPS plots, compositional data from XPS analysis, TR-PL decay fits, PL modelling parameters, additional PL spectra and maps.

AUTHOR INFORMATION

Corresponding Author

Philip Schulz

Email : philip.schulz@cnrs.fr

Author Contributions

The manuscript was written through contributions of all authors. All authors have given approval to the final version of the manuscript. † These authors contributed equally.

Notes

The authors declare no competing financial interest.

ACKNOWLEDGMENT

S.C. thanks funding from the European Union's Horizon 2020 research and innovation programme under the Marie Skłodowoska- Curie Grant Agreement N845612. This work was supported by the French government in the frame or the program of investments for the future (Programme d'Investissement d'Avenir ANR-IEED-002-01).

REFERENCES

(1) Correa-Baena, J.-P.; Saliba, M.; Buonassisi, T.; Grätzel, M.; Abate, A.; Tress, W.; Hagfeldt, A. Promises and Challenges of Perovskite Solar Cells. *Science* **2017**, *358* (6364), 739–744. https://doi.org/10.1126/science.aam6323.

(2) Park, N.-G.; Grätzel, M.; Miyasaka, T.; Zhu, K.; Emery, K. Towards Stable and Commercially Available Perovskite Solar Cells. *Nature Energy* **2016**, *1* (11), 16152. https://doi.org/10.1038/nenergy.2016.152.

(3) Jeong, J.; Kim, M.; Seo, J.; Lu, H.; Ahlawat, P.; Mishra, A.; Yang, Y.; Hope, M. A.; Eickemeyer, F. T.; Kim, M.; Yoon, Y. J.; Choi, I. W.; Darwich, B. P.; Choi, S. J.; Jo, Y.; Lee, J. H.; Walker, B.; Zakeeruddin, S. M.; Emsley, L.; Rothlisberger, U.; Hagfeldt, A.; Kim, D. S.; Grätzel, M.; Kim, J. Y. Pseudo-Halide Anion Engineering for α-FAPbI3 Perovskite Solar Cells. *Nature* **2021**, *592* (7854), 381–385. https://doi.org/10.1038/s41586-021-03406-5.

(4) Xiang, W.; Liu, S. (Frank); Tress, W. A Review on the Stability of Inorganic Metal Halide Perovskites: Challenges and Opportunities for Stable Solar Cells. *Energy Environ. Sci.* **2021**, *14* (4), 2090–2113. https://doi.org/10.1039/D1EE00157D.

(5) Khenkin, M. V.; Katz, E. A.; Abate, A.; Bardizza, G.; Berry, J. J.; Brabec, C.; Brunetti, F.; Bulović, V.; Burlingame, Q.; Di Carlo, A.; Cheacharoen, R.; Cheng, Y.-B.; Colsmann, A.; Cros, S.; Domanski, K.; Dusza, M.; Fell, C. J.; Forrest, S. R.; Galagan, Y.; Di Girolamo, D.; Grätzel, M.; Hagfeldt, A.; von Hauff, E.; Hoppe, H.; Kettle, J.; Köbler, H.; Leite, M. S.; Liu, S. (Frank); Loo, Y.-L.; Luther, J. M.; Ma, C.-Q.; Madsen, M.; Manceau, M.; Matheron, M.; McGehee, M.; Meitzner, R.; Nazeeruddin, M. K.; Nogueira, A. F.; Odabaşı, Ç.; Osherov, A.; Park, N.-G.; Reese, M. O.; De Rossi, F.; Saliba, M.; Schubert, U. S.; Snaith, H. J.; Stranks, S. D.; Tress, W.; Troshin, P. A.; Turkovic, V.; Veenstra, S.; Visoly-Fisher, I.; Walsh, A.; Watson, T.; Xie, H.; Yıldırım, R.; Zakeeruddin, S. M.; Zhu, K.; Lira-Cantu, M. Consensus Statement for Stability Assessment and Reporting for Perovskite Photovoltaics Based on ISOS Procedures. *Nat Energy* **2020**, *5* (1), 35–49. https://doi.org/10.1038/s41560-019-0529-5.

(6) Schulz, P.; Cahen, D.; Kahn, A. Halide Perovskites: Is It All about the Interfaces? *Chemical Reviews* **2019**, *119* (5), 3349–3417. https://doi.org/10.1021/acs.chemrev.8b00558.

(7) Li, C.; Tscheuschner, S.; Paulus, F.; Hopkinson, P. E.; Kießling, J.; Köhler, A.; Vaynzof, Y.; Huettner, S. Iodine Migration and Its Effect on Hysteresis in Perovskite Solar Cells. *Advanced Materials* **2016**, *28* (12), 2446–2454. https://doi.org/10.1002/adma.201503832.

(8) Grancini, G.; Roldán-Carmona, C.; Zimmermann, I.; Mosconi, E.; Lee, X.; Martineau, D.; Narbey, S.; Oswald, F.; De Angelis, F.; Graetzel, M.; Nazeeruddin, M. K. One-Year Stable

Perovskite Solar Cells by 2D/3D Interface Engineering. *Nature Communications* **2017**, *8*, 15684. https://doi.org/10.1038/ncomms15684.

(9) Noel, N. K.; Habisreutinger, S. N.; Wenger, B.; Lin, Y.-H.; Zhang, F.; Patel, J. B.; Kahn, A.; Johnston, M. B.; Snaith, H. J. Elucidating the Role of a Tetrafluoroborate-Based Ionic Liquid at the n-Type Oxide/Perovskite Interface. *Advanced Energy Materials* **2020**, *10* (4), 1903231. https://doi.org/10.1002/aenm.201903231.

(10) Zhumagali, S.; Isikgor, F. H.; Maity, P.; Yin, J.; Ugur, E.; De Bastiani, M.; Subbiah, A. S.; Mirabelli, A. J.; Azmi, R.; Harrison, G. T.; Troughton, J.; Aydin, E.; Liu, J.; Allen, T.; Rehman, A. ur; Baran, D.; Mohammed, O. F.; De Wolf, S. Linked Nickel Oxide/Perovskite Interface Passivation for High-Performance Textured Monolithic Tandem Solar Cells. *Advanced Energy Materials n/a* (n/a), 2101662. https://doi.org/10.1002/aenm.202101662.

(11) Xing, G.; Mathews, N.; Sun, S.; Lim, S. S.; Lam, Y. M.; Gratzel, M.; Mhaisalkar, S.; Sum, T. C. Long-Range Balanced Electron- and Hole-Transport Lengths in Organic-Inorganic CH3NH3PbI3. *Science* **2013**, *342* (6156), 344–347. https://doi.org/10.1126/science.1243167.

(12) Steirer, K. X.; Schulz, P.; Teeter, G.; Stevanovic, V.; Yang, M.; Zhu, K.; Berry, J. J. Defect Tolerance in Methylammonium Lead Triiodide Perovskite. *ACS Energy Letters* **2016**, *1* (2), 360–366. https://doi.org/10.1021/acsenergylett.6b00196.

(13) Cho, A.-N.; Park, N.-G. Impact of Interfacial Layers in Perovskite Solar Cells. *ChemSusChem* **2017**, *10* (19), 3687–3704. https://doi.org/10.1002/cssc.201701095.

(14) Fakharuddin, A.; Schmidt-Mende, L.; Garcia-Belmonte, G.; Jose, R.; Mora-Sero, I. Interfaces in Perovskite Solar Cells. *Advanced Energy Materials* **2017**, *7* (22), 1700623. https://doi.org/10.1002/aenm.201700623.

(15) Qiu, L.; Ono, L. K.; Jiang, Y.; Leyden, M. R.; Raga, S. R.; Wang, S.; Qi, Y. Engineering Interface Structure to Improve Efficiency and Stability of Organometal Halide Perovskite Solar Cells. *J. Phys. Chem. B* **2018**, *122* (2), 511–520. https://doi.org/10.1021/acs.jpcb.7b03921.

(16) Domanski, K.; Correa-Baena, J.-P.; Mine, N.; Nazeeruddin, M. K.; Abate, A.; Saliba, M.; Tress, W.; Hagfeldt, A.; Grätzel, M. Not All That Glitters Is Gold: Metal-Migration-Induced Degradation in Perovskite Solar Cells. *ACS Nano* **2016**, *10* (6), 6306–6314. https://doi.org/10.1021/acsnano.6b02613.

(17) Cacovich, S.; Ciná, L.; Matteocci, F.; Divitini, G.; Midgley, P. A.; Di Carlo, A.; Ducati, C. Gold and Iodine Diffusion in Large Area Perovskite Solar Cells under Illumination. *Nanoscale* **2017**, *9* (14), 4700–4706. https://doi.org/10.1039/C7NR00784A.

(18) Kim, S.; Bae, S.; Lee, S.-W.; Cho, K.; Lee, K. D.; Kim, H.; Park, S.; Kwon, G.; Ahn, S.-W.; Lee, H.-M.; Kang, Y.; Lee, H.-S.; Kim, D. Relationship between Ion Migration and Interfacial Degradation of CH3NH3PbI3 Perovskite Solar Cells under Thermal Conditions. *Sci Rep* **2017**, *7* (1), 1200. https://doi.org/10.1038/s41598-017-00866-6.

(19) Li, Z.; Xiao, C.; Yang, Y.; Harvey, S. P.; Kim, D. H.; Christians, J. A.; Yang, M.; Schulz, P.; Nanayakkara, S. U.; Jiang, C.-S.; Luther, J. M.; Berry, J. J.; Beard, M. C.; Al-Jassim, M. M.; Zhu, K. Extrinsic Ion Migration in Perovskite Solar Cells. *Energy Environ. Sci.* **2017**, *10* (5), 1234–1242. https://doi.org/10.1039/C7EE00358G.

(20) Jeangros, Q.; Duchamp, M.; Werner, J.; Kruth, M.; Dunin-Borkowski, R. E.; Niesen, B.; Ballif, C.; Hessler-Wyser, A. In Situ TEM Analysis of Organic–Inorganic Metal-Halide Perovskite Solar Cells under Electrical Bias. *Nano Letters* **2016**, *16* (11), 7013–7018. https://doi.org/10.1021/acs.nanolett.6b03158.

(21) Cacovich, S.; Matteocci, F.; Abdi-Jalebi, M.; Stranks, S. D.; Di Carlo, A.; Ducati, C.; Divitini, G. Unveiling the Chemical Composition of Halide Perovskite Films Using Multivariate Statistical Analyses. *ACS Appl. Energy Mater.* **2018**, *1* (12), 7174–7181. https://doi.org/10.1021/acsaem.8b01622.

(22) Harvey, S. P.; Messinger, J.; Zhu, K.; Luther, J. M.; Berry, J. J. Investigating the Effects of Chemical Gradients on Performance and Reliability within Perovskite Solar Cells with TOF-SIMS. *Advanced Energy Materials* **2020**, *10* (26), 1903674. https://doi.org/10.1002/aenm.201903674.

(23) Zhang, T.; Meng, X.; Bai, Y.; Xiao, S.; Hu, C.; Yang, Y.; Chen, H.; Yang, S. Profiling the Organic Cation-Dependent Degradation of Organolead Halide Perovskite Solar Cells. *J. Mater. Chem. A* **2017**, *5* (3), 1103–1111. https://doi.org/10.1039/C6TA09687E.

(24) Ralaiarisoa, M.; Busby, Y.; Frisch, J.; Salzmann, I.; Pireaux, J.-J.; Koch, N. Correlation of Annealing Time with Crystal Structure, Composition, and Electronic Properties of CH3NH3PbI3−xClx Mixed-Halide Perovskite Films. *Phys. Chem. Chem. Phys.* **2016**, *19* (1), 828–836. https://doi.org/10.1039/C6CP06347K.

(25) Lee, H.; Gaiaschi, S.; Chapon, P.; Marronnier, A.; Lee, H.; Vanel, J.-C.; Tondelier, D.; Bourée, J.-E.; Bonnassieux, Y.; Geffroy, B. Direct Experimental Evidence of Halide Ionic Migration under Bias in $CH_3NH_3PbI_{3-x}Cl_x$ -Based Perovskite Solar Cells Using GD-OES Analysis. *ACS Energy Letters* **2017**, *2* (4), 943–949. https://doi.org/10.1021/acsenergylett.7b00150.

(26) Ahmad, Z.; Najeeb, M. A.; Shakoor, R. A.; Alashraf, A.; Al-Muhtaseb, S. A.; Soliman, A.; Nazeeruddin, M. K. Instability in CH3NH3PbI3 Perovskite Solar Cells Due to Elemental

Migration and Chemical Composition Changes. *Sci Rep* **2017**, *7* (1), 15406. https://doi.org/10.1038/s41598-017-15841-4.

(27) Das, C.; Wussler, M.; Hellmann, T.; Mayer, T.; Jaegermann, W. *In Situ* XPS Study of the Surface Chemistry of MAPI Solar Cells under Operating Conditions in Vacuum. *Physical Chemistry Chemical Physics* **2018**, *20* (25), 17180–17187. https://doi.org/10.1039/C8CP01259H.

(28) Das, C.; Wussler, M.; Hellmann, T.; Mayer, T.; Zimmermann, I.; Maheu, C.; Nazeeruddin, M. K.; Jaegermann, W. Surface, Interface, and Bulk Electronic and Chemical Properties of Complete Perovskite Solar Cells: Tapered Cross-Section Photoelectron Spectroscopy, a Novel Solution. *ACS Appl. Mater. Interfaces* **2020**, *12* (36), 40949–40957. https://doi.org/10.1021/acsami.0c11484.

(29) Yuan, H.; Debroye, E.; Janssen, K.; Naiki, H.; Steuwe, C.; Lu, G.; Moris, M.; Orgiu, E.; Uji-i, H.; De Schryver, F.; Samorì, P.; Hofkens, J.; Roeffaers, M. Degradation of Methylammonium Lead Iodide Perovskite Structures through Light and Electron Beam Driven Ion Migration. *The Journal of Physical Chemistry Letters* **2016**, *7* (3), 561–566. https://doi.org/10.1021/acs.jpclett.5b02828.

(30) Kosasih, F. U.; Cacovich, S.; Divitini, G.; Ducati, C. Nanometric Chemical Analysis of Beam-Sensitive Materials: A Case Study of STEM-EDX on Perovskite Solar Cells. *Small Methods* **2020**, 2000835. https://doi.org/10.1002/smtd.202000835.

(31) Noël, C.; Pescetelli, S.; Agresti, A.; Franquet, A.; Spampinato, V.; Felten, A.; di Carlo, A.; Houssiau, L.; Busby, Y. Hybrid Perovskites Depth Profiling with Variable-Size Argon Clusters and Monatomic Ions Beams. *Materials* **2019**, *12* (5), 726. https://doi.org/10.3390/ma12050726.

(32) Klein-Kedem, N.; Cahen, D.; Hodes, G. Effects of Light and Electron Beam Irradiation on Halide Perovskites and Their Solar Cells. *Accounts of Chemical Research* **2016**, *49* (2), 347–354. https://doi.org/10.1021/acs.accounts.5b00469.

(33) Béchu, S.; Ralaiarisoa, M.; Etcheberry, A.; Schulz, P. Photoemission Spectroscopy Characterization of Halide Perovskites. *Adv. Energy Mater.* **2020**, 1904007. https://doi.org/10.1002/aenm.201904007.

(34) Hofstetter, Y. J.; Vaynzof, Y. Quantifying the Damage Induced by X-Ray Photoelectron Spectroscopy Depth Profiling of Organic Conjugated Polymers. *ACS Appl. Polym. Mater.* **2019**, *1* (6), 1372–1381. https://doi.org/10.1021/acsapm.9b00148.

(35) Svanström, S.; Fernández, A. G.; Sloboda, T.; Jacobsson, T. J.; Rensmo, H.; Cappel, U. B. X-Ray Stability and Degradation Mechanism of Lead Halide Perovskites and Lead Halides. *Phys. Chem. Chem. Phys.* **2021**, *23* (21), 12479–12489. https://doi.org/10.1039/D1CP01443A.

(36) Cacovich, S.; Messou, D.; Bercegol, A.; Béchu, S.; Yaiche, A.; Shafique, H.; Rousset, J.; Schulz, P.; Bouttemy, M.; Lombez, L. Light-Induced Passivation in Triple Cation Mixed Halide Perovskites: Interplay between Transport Properties and Surface Chemistry. *ACS Appl. Mater. Interfaces* **2020**, *12* (31), 34784–34794. https://doi.org/10.1021/acsami.0c06844.

(37) Philippe, B.; Saliba, M.; Correa-Baena, J.-P.; Cappel, U. B.; Turren-Cruz, S.-H.; Grätzel, M.; Hagfeldt, A.; Rensmo, H. Chemical Distribution of Multiple Cation (Rb^+, Cs^+, MA^+, and FA^+) Perovskite Materials by Photoelectron Spectroscopy. *Chemistry of Materials* **2017**, *29* (8), 3589–3596. https://doi.org/10.1021/acs.chemmater.7b00126.

(38) McGettrick, J. D.; Hooper, K.; Pockett, A.; Baker, J.; Troughton, J.; Carnie, M.; Watson, T. Sources of Pb(0) Artefacts during XPS Analysis of Lead Halide Perovskites. *Materials Letters* **2019**, *251*, 98–101. https://doi.org/10.1016/j.matlet.2019.04.081.

(39) Li, Y.; Xu, X.; Wang, C.; Ecker, B.; Yang, J.; Huang, J.; Gao, Y. Light-Induced Degradation of $CH_3NH_3PbI_3$ Hybrid Perovskite Thin Film. *The Journal of Physical Chemistry C* **2017**, *121* (7), 3904–3910. https://doi.org/10.1021/acs.jpcc.6b11853.

(40) Bouttemy, M.; Béchu, S.; Spencer, B. F.; Dally, P.; Chapon, P.; Etcheberry, A. Combined Pulsed RF GD-OES and HAXPES for Quantified Depth Profiling through Coatings. *Coatings* **2021**, *11* (6), 702. https://doi.org/10.3390/coatings11060702.

(41) Das, C.; Zia, W.; Mortan, C.; Hussain, N.; Saliba, M.; Flege, J. I.; Kot, M. Top Down Approach to Study Chemical and Electronic Properties of Perovskite Solar Cells: Sputtered Depth Profiling Versus Tapered Cross-Section Photoelectron Spectroscopy. *Solar RRL n/a* (n/a). https://doi.org/10.1002/solr.202100298.

(42) Zhang, W.; Saliba, M.; Moore, D. T.; Pathak, S. K.; Hörantner, M. T.; Stergiopoulos, T.; Stranks, S. D.; Eperon, G. E.; Alexander-Webber, J. A.; Abate, A.; Sadhanala, A.; Yao, S.; Chen, Y.; Friend, R. H.; Estroff, L. A.; Wiesner, U.; Snaith, H. J. Ultrasmooth Organic–Inorganic Perovskite Thin-Film Formation and Crystallization for Efficient Planar Heterojunction Solar Cells. *Nat Commun* **2015**, *6* (1), 6142. https://doi.org/10.1038/ncomms7142.

(43) Delamarre, A.; Lombez, L.; Guillemoles, J.-F. Contactless Mapping of Saturation Currents of Solar Cells by Photoluminescence. *Applied Physics Letters* **2012**, *100* (13), 131108. https://doi.org/10.1063/1.3697704.

(44) Bercegol, A.; El-Hajje, G.; Ory, D.; Lombez, L. Determination of Transport Properties in Optoelectronic Devices by Time-Resolved Fluorescence Imaging. *Journal of Applied Physics* **2017**, *122* (20), 203102. https://doi.org/10.1063/1.5005164.

(45) Katahara, J. K.; Hillhouse, H. W. Quasi-Fermi Level Splitting and Sub-Bandgap Absorptivity from Semiconductor Photoluminescence. *Journal of Applied Physics* **2014**, *116* (17), 173504. https://doi.org/10.1063/1.4898346.

(46) Kirchartz, T.; Márquez, J. A.; Stolterfoht, M.; Unold, T. Photoluminescence-Based Characterization of Halide Perovskites for Photovoltaics. *Adv. Energy Mater.* **2020**, 1904134. https://doi.org/10.1002/aenm.201904134.

(47) Maiberg, M.; Scheer, R. Theoretical Study of Time-Resolved Luminescence in Semiconductors. II. Pulsed Excitation. *Journal of Applied Physics* **2014**, *116* (12), 123711. https://doi.org/10.1063/1.4896484.

(48) Vidon, G.; Cacovich, S.; Legrand, M.; Yaiche, A.; Ory, D.; Suchet, D.; Puel, J.-B.; Guillemoles, J.-F. Mapping Transport Properties of Halide Perovskites via Short-Time-Dynamics Scaling Laws and Subnanosecond-Time-Resolution Imaging. *Phys. Rev. Applied* **2021**, *16* (4), 044058. https://doi.org/10.1103/PhysRevApplied.16.044058.

TOC

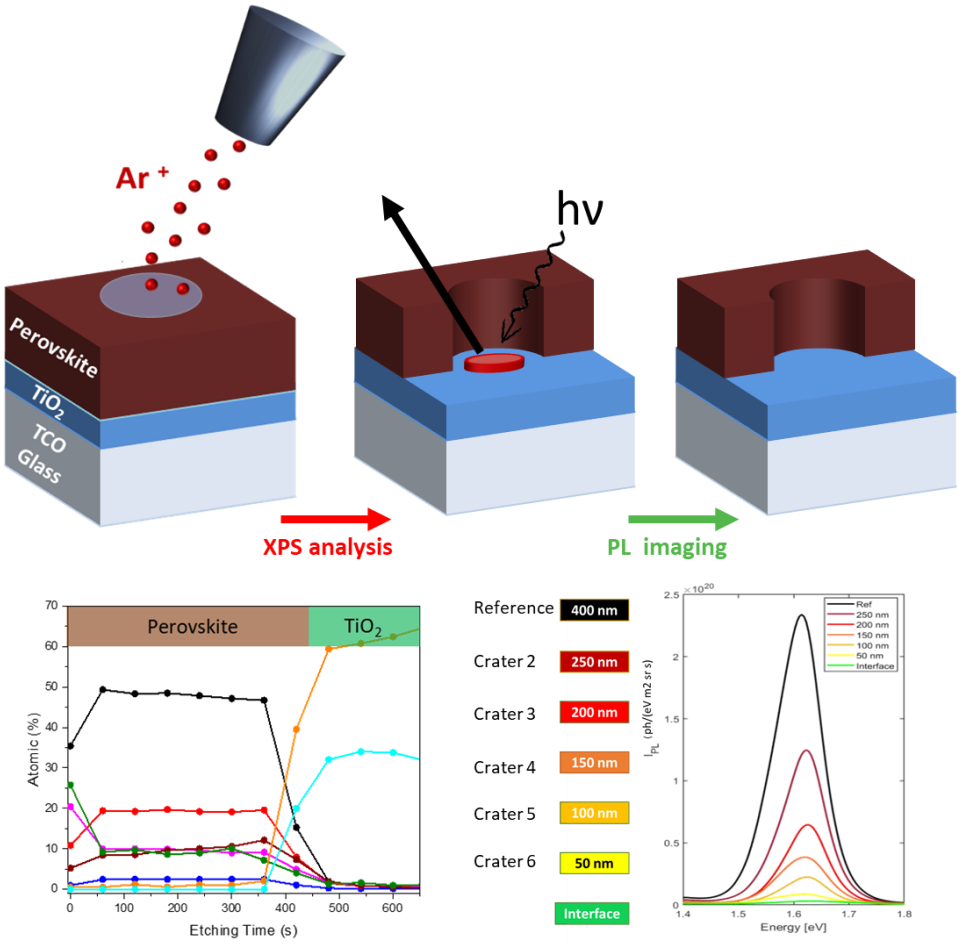
Ar +
hν
Perovskite
TiO2
TCO
Glass
XPS analysis
PL imaging
Perovskite
TiO2
Atomic (%)
Etching Time (s)
Reference
Crater 2
Crater 3
Crater 4
Crater 5
Crater 6
400 nm
250 nm
200 nm
150 nm
100 nm
50 nm
Interface
Ref
250 nm
200 nm
150 nm
100 nm
50 nm
Interface
Energy [eV]